





PAPER

[View Article Online](#)
[View Journal](#) | [View Issue](#)Cite this: *Dalton Trans.*, 2023, **52**, 14017

Structural variation, magnetism and single-source deposition of lanthanide-containing polyoxotitanates†

Rosa Müller, Olivia Georghiades, Joshua D. Bocarsly, Farheen N. Sayed, Víctor Riesgo-González,  Andrew D. Bond,  Clare P. Grey  and Dominic S. Wright *

Heterometal-containing polyoxotitanates (POTs) are much-studied single-source precursors (SSPs) for doped TiO_2 . In this work the properties of a wide range of lanthanide-containing POTs are studied to assess their potential use as SSPs for Ln–Ti hybrid oxides. The novel cage compounds $\{[\text{Ti}_2\text{O}(\text{OEt})_8](\text{EtOH}\cdot\text{LnCl})_2\}$ (Ln = Sm, Gd, Tb, Dy, Ho, Tm and Yb) are structurally characterised. The magnetic properties of the Ln = Dy and Ho compounds were characterised using SQUID magnetometry—in both cases, there is evidence of significant uniaxial magnetic anisotropy, but magnetic relaxation is fast and therefore no single-molecule magnetic properties are observed. Upon decomposition lanthanide-doped anatase (Ln = La) or titania/LnTi–oxide mixtures are obtained, which show efficient stabilisation of the catalytically active anatase phase up to high temperatures, making the materials of potential interest for applications in photocatalysis.

Received 7th August 2023,
Accepted 14th September 2023

DOI: 10.1039/d3dt02553e

rsc.li/dalton

1. Introduction

Titanium dioxide is a versatile, abundant and non-toxic high band gap semiconductor used in a multitude of applications.¹ Its photocatalytic activity means that it has found important uses in photovoltaics, sensors, photochromic devices, and as a photocatalyst in water splitting.² Due to the wide band gap of titanium dioxide (3.20 eV direct band gap for anatase)³ many of these technologies are limited to the absorption of UV light. However, the introduction of dopant metal ions reduces the band gap due to the introduction of additional states above the valence band, which leads to higher efficiencies using ambient light.⁴ In addition to first-row transition metals such as Fe, Co or Cu, f-block elements (lanthanides) are also suitable dopants, and lead to enhanced properties of the resulting titania materials.⁵ Early lanthanides (La, Ce) are reported to stabilise the thermodynamically less stable, but highly catalytically active, anatase phase of TiO_2 by suppressing the thermal anatase-to-rutile phase transition.⁶ Furthermore the presence

of hard lanthanide ions promotes interactions with Lewis basic functionalities (such as acids, aldehydes or alcohols) which are present in organic pollutants.⁷ Hence, the resulting materials are promising candidates for photocatalytic degradation applications.

When the Ln ratio is increased, a series of mixed-metal oxides of general formulae $\text{Ln}_2\text{Ti}_2\text{O}_7$ can also be formed. These compounds can adopt closely related pyrochlore or fluorite structures which differ in the extent of cation mixing, where the stability window of the ‘ideal’ pyrochlores ($\text{A}_2\text{B}_2\text{O}_7$, in which no cation mixing is present) can be predicted using the radius ratio of the cations (r_A/r_B).^{9a} It is well established, however, that the degree of cation and anion mixing in these species is very dependent on synthetic conditions employed.^{9b} Pyrochlores have a range of desirable properties depending on their composition, and have found uses as luminescence materials, catalysts, nuclear waste immobilization materials and as ionic and electrical conductors. For simplicity, here we will use the term ‘pyrochlore-like’ generically to describe compounds of formula $\text{Ln}_2\text{Ti}_2\text{O}_7$ in the text.

Pyrochlore-like $\text{Ln}_2\text{Ti}_2\text{O}_7$ compounds can have a range of desirable chemical and physical properties. Owing to their non-centrosymmetric structures $\text{La}_2\text{Ti}_2\text{O}_7$ and $\text{Nd}_2\text{Ti}_2\text{O}_7$ are ferroelectric materials analogous to $\text{Cd}_2\text{Nb}_2\text{O}_7$ and are also suitable components for high-temperature microwave dielectric materials.¹⁰ Due to the increasing number of unpaired electrons, pyrochlore-like compounds containing later lantha-

The Yusuf Hamied Department of Chemistry, Cambridge University, Lensfield Road, Cambridge CB2 1EW, UK. E-mail: dsw1000@cam.ac.uk; Tel: +44 (0)1223 763122

†Electronic supplementary information (ESI) available: Crystallographic data, CShM analysis, Raman spectra, AC susceptibility data, EDX/SEM results and details of the Rietveld refinement. CCDC 2283715–2283722. For ESI and crystallographic data in CIF or other electronic format see DOI: <https://doi.org/10.1039/d3dt02553e>

nides show unusual antiferromagnetic (Ln = Eu–Er) and ferromagnetic (Ln = Yb) behaviour as well as abnormal luminescence (Ln = Eu) and oxygen-ion conductivity (Ln = Gd).¹¹

Common synthetic strategies to prepare lanthanide-containing titania include sol-gel methods and high-temperature sintering of $\text{Ln}_2\text{O}_3/\text{TiO}_2$ mixtures.⁸ Given the large impact of the metal-dopant level on the properties of TiO_2 -based materials a high level of stoichiometric control is required in their synthesis. The use of molecular single-source precursors (SSPs) allows precise control over dopant concentration, distribution and connectivity in the bulk materials.¹² A class of suitable SSPs for this purpose are polyoxotitanates (POTs) of the general form $[\text{Ti}_x\text{O}_y(\text{OR})_z\text{M}_n]$ which have been widely studied as SSPs for transition metal-doped titania.¹³ We have previously reported a series of lanthanide-containing POTs obtained *via* solvothermal reactions of $\text{Ti}(\text{OEt})_4$ with LnCl_3 in ethanol. The high-nuclearity cage arrangement $[\text{Ti}_{28}\text{O}_{38}(\text{OEt})_{40}\text{H}_2\text{LnCl}]$ (**Ti₂₈Ln**, Fig. 1a) was obtained for the early lanthanides (Ln = La, Ce), a structure whose TiO core offers a high coordination number for the lanthanide ions.¹⁴ In the case of Ce, further analysis of the reaction mixture showed the formation of two smaller cages, $[\text{Ti}_8\text{O}_7(\text{OEt})_{21}(\text{EtOH}\cdot\text{Ce})]$ (**Ti₈Ln**) and $[\{\text{Ti}_2\text{O}(\text{OEt})_8\}(\text{EtOH}\cdot\text{CeCl})]_2$ (**Ti₄Ln₂**) (Fig. 1b and c, respectively).¹⁵ However, moving along the lanthanide series to the slightly smaller lanthanides Nd and Eu, only the **Ti₄Ln₂** cages were obtained.¹⁶ This trend indicates the dependency of the preferred structure on the coordination geometry and the ionic radius of the lanthanide ion, which is a well-known feature of various classes of Ln-compounds.¹⁷ Interestingly, for Er this trend towards lower nuclearity cages is disrupted, as the main reaction product is the **Ti₈Er**-cage.¹⁸ Decomposition of the Ce and Eu-containing cages as SSPs gives either Ln-doped TiO_2 for low Ti:Ln ratios (28:1 and 8:1, *i.e.* **Ti₂₈Ln** and **Ti₈Ln**), or TiO_2 -stabilised $\text{Ln}_2\text{Ti}_2\text{O}_7$ for higher ratios (2:1, *i.e.* **Ti₄Ln₂**).

In this work we explore the structural variation of alkoxy-substituted Ln-POTs with a broader range of lanthanide ions [Ln = Sm (**Ti₄Sm₂**), Gd (**Ti₄Gd₂**), Tb (**Ti₄Tb₂**), Dy (**Ti₄Dy₂**), Ho

(**Ti₄Ho₂**), Tm (**Ti₄Tm₂**) and Yb (**Ti₄Yb₂**)] and their applications as SSPs for the respective $\text{Ln}_2\text{Ti}_2\text{O}_7$ pyrochlore-like materials. We identify and quantify the phases formed upon the hydrolytic decomposition of each of the cages using synchrotron powder X-ray diffraction and compare the results to those obtained for the literature-known compounds **Ti₂₈La**, **Ti₄Ce₂**, **Ti₄Nd₂**, **Ti₄Eu₂** and **Ti₈Er**. Some unexpected solid-state products, namely $\text{Nd}_4\text{Ti}_9\text{O}_{24}$ from the Nd cage **Ti₄Nd₂** and Ce(IV) oxides from the Ce cage **Ti₄Ce₂**, are identified. Furthermore, the magnetic properties of **Ti₄Dy₂** and **Ti₄Ho₂** are investigated to assess the possibility of single-molecule magnetism (SMM). This study provides a better understanding of the nature of these cages as SSPs and highlights their potentially diverse applications in materials synthesis.

2. Results and discussion

Synthesis of Ln-POTs

The desired Ln-POTs were obtained *via* solvothermal reactions of $\text{Ti}(\text{OEt})_4$ with the respective $\text{Ln}(\text{m})\text{Cl}_3$ salts (Ln = Sm, Gd, Tb, Dy, Ho, Tm and Yb) in anhydrous ethanol at 180 °C in an autoclave, following a procedure described in our previous paper.¹⁵ All the products were shown to be of the type **Ti₄Ln₂**, $[\{\text{Ti}_2\text{O}(\text{OEt})_8\}(\text{EtOH}\cdot\text{LnCl})]_2$ by powder and single-crystal XRD. Due to the paramagnetic nature of the cages NMR spectroscopy was not of any value in their characterisation. In addition, mass spectrometry only revealed minor fragments together with presumed hydrolysis products. In general, yields decreased with decreasing ionic radius of the Ln^{3+} ion, which can potentially be attributed to an increase in structural strain in accommodating the Ln^{3+} ions (see the structural discussion below). The formation of solid products was only observed for Ti (OEt)₄:LnCl₃ reaction stoichiometries as high as 5:1. When $\text{Ti}(\text{OEt})_4$ was replaced with $\text{Ti}(\text{O}^i\text{Pr})_4$ using ethanol as the reaction solvent the same ethoxy-substituted compounds were formed, illustrating significant ligand exchange at the cage periphery with the solvent. Interestingly, no major contamination with biproducts such as $[\text{Ti}_{16}\text{O}_{16}(\text{OEt})_{32}]$ was observed in any of these reactions, as observed in our previous report.¹⁴

An influence of the anion in LnX_3 on the resulting cage structure has been described for similar solvothermal reactions.¹⁹ We find that this is also the case here. For example, the reaction of $\text{Eu}(\text{OAc})_3$ with $\text{Ti}(\text{OEt})_4$ gives a cage isostructural with $[\text{Ti}_4\text{O}(\text{OEt})_{15}\text{Cu}(\text{Cl})]$ (CSD: EWONIO), as confirmed by the crystallographic unit-cell parameters. This structural type has previously been reported for the ethoxy-cages of first-row transition metals using MCl_2 precursors (M = Co, Zn, Fe, Cu).¹³

Single-crystal X-ray structures

The reaction conditions were modified to investigate formation of the different cage types shown in Fig. 1. Eight new cages $[\{\text{Ti}_2\text{O}(\text{OEt})_8\}(\text{EtOH}\cdot\text{LnCl})]_2$ [Ln = Sm (**Ti₄Sm₂**), Gd (**Ti₄Gd₂**), Tb (**Ti₄Tb₂**), Dy (**Ti₄Dy₂**), Ho (**Ti₄Ho₂**), Tm (**Ti₄Tm₂**), Yb (**Ti₄Yb₂**)] were structurally characterised in the current study. The analogous structures of **Ti₄Ce₂**, **Ti₄Nd₂** and **Ti₄Eu₂**

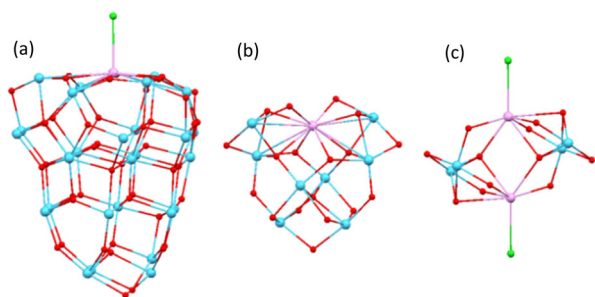


Fig. 1 The three different structural types (a) **Ti₂₈Ln**, (b) **Ti₈Ln** and (c) **Ti₄Ln₂** of ethoxy-substituted Ln-POTs, with ligands omitted for clarity. A consistent colour scheme of Ln = pink, Ti = blue, O = red, Cl = green is used throughout this paper. Structural data were obtained from the CSD (**Ti₂₈La** = DEJQUG, **Ti₈Ln** = ORIFAY, **Ti₄Eu₂** = CURJEG). For (b), the structure containing Ce (**Ti₈Ce** = ZIWYAI) has a further EtOH molecule coordinated to the lanthanide centre.



have been reported previously.^{15,16} The molecular structure of all of these cages is centrosymmetric (Fig. 2), with the asymmetric unit containing two face-sharing TiO_6 octahedra and with the Ln^{3+} ion situated in a “pocket” above two faces (Fig. 3). Two $\{\text{Ti}_2\text{O}(\text{OEt})_8\}(\text{EtOH}\cdot\text{LnCl})$ subunits come together so that Ln^{3+} ion in one unit bridges an edge of a TiO_6 octahedron of the other. The Ln^{3+} ions adopt overall a distorted 8-coordinate geometry (ESI, Fig. S4†).

The fact that the $\{\text{Ti}_2\text{O}(\text{OEt})_8\}$ fragments in the Ti_4Ln_2 cage are held together solely by the bridging Ln^{3+} ions (they are not directly linked through Ti–O bonds) provides a flexible molecular geometry. To quantify the structural strain imposed on the TiO_6 octahedra across the series, we considered the continuous shape measure (CShM) relative to a centred regular octahedron.²⁰ A CShM value of zero indicates perfect octahedral symmetry, while an increasing value indicates increasing deviation from regularity (ESI, Tables S2, S3 and S7†). It is evident that the TiO_6 octahedron involved in the edge-sharing contact with Ln^{3+} is more distorted than the other TiO_6 octahedron in the face-sharing pair, and its CShM value also increases more rapidly across the series. The degree of structural strain in the $\{\text{Ti}_2\text{O}(\text{OEt})_8\}$ fragments increases as Ln^{3+} gets smaller, but the molecular flexibility is evidently sufficient to permit formation of this cage type across the entire Ln series.

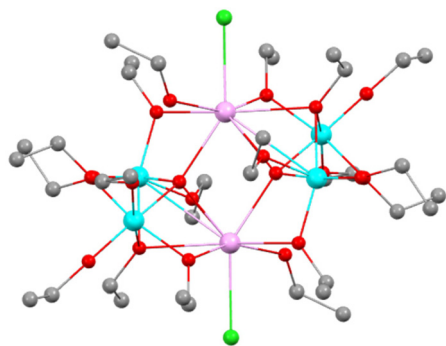


Fig. 2 Single-crystal X-ray structure of $[\{\text{Ti}_2\text{O}(\text{OEt})_8\}(\text{EtOH}\cdot\text{SmCl})]_2$ (Ti_4Sm_2) with hydrogen atoms omitted for clarity. The other novel compounds (Ti_4Gd_2 , Ti_4Tb_2 , Ti_4Dy_2 , Ti_4Ho_2 , Ti_4Er_2 , Ti_4Tm_2 and Ti_4Yb_2) reported in this work are isostructural. (Ln = pink, Ti = blue, O = red, Cl = green). Full details of the data collections, refinements, and bond lengths and angles can be found in the ESI.†

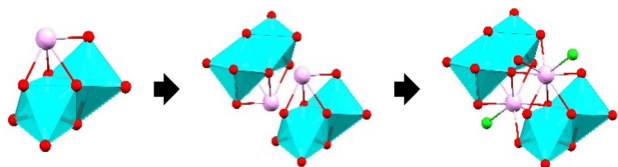


Fig. 3 Schematic representation of the structural units in Ti_4Ln_2 . Ln^{3+} sits above two faces of the face-sharing TiO_6 octahedra, and pairs of these units come together with Ln^{3+} bridging an edge of the neighbouring TiO_6 octahedron.

The previously reported Ti_8Ln (Ln = Ce or Er) cages contain the same face-sharing $\{\text{Ti}_2\text{O}(\text{OEt})_8\}$ fragments as Ti_4Ln_2 , but they adopt a “tetrahedral” arrangement around a single Ln^{3+} ion (Fig. 4).¹⁵ The location of Ln^{3+} relative to the face-sharing TiO_6 octahedra is equivalent to that in Ti_4Ln_2 . The existence of these common $\{\text{Ti}_2\text{O}(\text{OEt})_8\}$ fragments in both Ti_4Ln_2 and Ti_8Ln suggest that these small units are likely to exist as precursors in solution. In Ti_8Ln , however, the $\{\text{Ti}_2\text{O}(\text{OEt})_8\}$ fragments are directly linked through four further TiO_6 octahedra in an edge-sharing arrangement. Hence, the Ti_8O_{28} framework in Ti_8Ln presents an inherently less flexible binding pocket for Ln^{3+} . In the Ti_8Ce cage, Ce^{3+} is accommodated with further coordination by an EtOH molecule, giving 9-coordination overall. In Ti_8Er , Er^{3+} is 8-coordinate with no further coordination. The CShM values for the TiO_6 octahedra in Ti_8Ln vary little between Ln = Ce and Er, consistent with the picture of an inherently less flexible framework.

It was shown previously that for Ln = Ce all three structural types are obtained upon fractional crystallisation, with the large Ti_{28}Ce cluster crystallising first, followed by Ti_8Ce and Ti_4Ce_2 , which could be separated by hand on the basis of their difference in colour.¹⁵ The presence of all three cage types for Ce suggests either simultaneous formation of all three products during the reaction or a dynamic equilibrium between them in solution. Consistent with the latter proposition, we have found in the current work that when the reaction mixture is cooled rapidly down to -30°C (instead of slowly from 180°C), the yellow crystalline product is exclusively the Ti_4Ce_2 cage (Fig. S2†). However, for Ln = La only the largest cage type is obtained (Ti_{28}La). Nd and later lanthanides appear to form the smallest Ti_4Ln_2 type cluster exclusively, with no indication of Ti_8Ln cage formation even after storing the reaction mixture at -30°C for several weeks. The late lanthanide Er is an exception to this trend, as it forms Ti_8Er as the main product. The preference for Er to adopt the Ti_8Er cage is consistent with size selectivity, which is optimal for Er^{3+} and is also able to accommodate Ce^{3+} with further EtOH coordination. Moving across the lanthanide series, the elements between Ce and Er may be too small to permit 9-coordination but too large to permit 8-coordination.

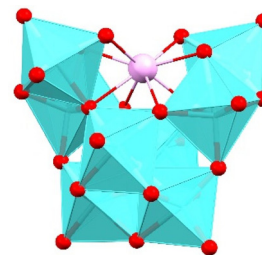


Fig. 4 Polyhedral representation of the Ti_8Ln cage (Ln = Er, CSD ORIFAY). Carbon and hydrogen atoms are omitted for clarity. Ln^{3+} is located between two pairs of face-sharing TiO_6 octahedra making a “tetrahedral” arrangement, further linked through four edge-sharing TiO_6 octahedra.



Within the larger Ti_{28}Ln cages (Ln = La, Ce), the TiO_6 octahedra adopt corner- and edge-sharing arrangements, with some additional 7-coordinate pentagonal-bipyramidal sites also present. Face-sharing TiO_6 octahedra are not seen. The Ln^{3+} ions are coordinated by a planar $\text{Ti}_6(\text{OEt})_6$ metallocrown fragment, giving a seven-coordinate, hexagonal-based pyramidal geometry. Again, the $\text{Ti}_{28}\text{O}_{39}$ cage is directly connected, and therefore is expected to show limited flexibility in its Ln^{3+} binding site. The arrangement is presumably unstable for the smaller Ln^{3+} ions after Ce^{3+} , leading to preference for the smaller Ti_8Ln and Ti_4Ln_2 cages.

Magnetic measurements

$\text{Ln}(\text{III})$ compounds with axial symmetry have often been observed to show single-molecule magnet behaviour, characterised by slow magnetic relaxation arising from a bistable magnetic ground state with a significant barrier to relaxation (U_{eff}). Therefore, the clusters reported here, which feature approximate axial symmetry along the $\text{Ln}^{3+}\text{--Ln}^{3+}$ axis, could be of potential interest for single-molecule magnetism.²¹

Our studies focused on the two rare earths with the highest total magnetic moments, Dy^{3+} ($f^9, J = 15/2$, a Kramers ion) and Ho^{3+} (f^{10} , a non-Kramers ion, $J = 8$). In particular, Dy^{3+} is known to show strong magnetic anisotropy and a bistable magnetic ground state owing to its Kramers nature, and therefore is the most likely lanthanide ion to result in single molecule magnet behaviour.²² The Ti^{4+} is d^0 , and therefore not expected to contribute to the magnetic moment in these compounds. DC magnetisation vs. field/temperature and AC susceptibility measurements were carried out for powdered samples of Ti_4Dy_2 and Ti_4Ho_2 using SQUID magnetometry. Plots of $\chi(T) \cdot T$ show that both compounds saturate to a constant value around $17.1 \text{ emu K Oe}^{-1} \text{ mol}^{-1}$, corresponding to an effective magnetic moment $\mu_{\text{eff}} = 11.7 \mu_{\text{B}}$ (Fig. 5a). The theoretical effective moments for Dy^{3+} and Ho^{3+} may be estimated according to $\mu_{\text{eff}} = g_J \sqrt{J(J+1)}$, where g_J is the Landé g -factor (1.33 for Dy^{3+} and $1.25 \mu_{\text{B}}$ for Ho^{3+}). This gives expected moments of $10.63 \mu_{\text{B}}$ for Dy^{3+} and $10.60 \mu_{\text{B}}$ for Ho^{3+} , in reasonable agreement with the experiment. Even better agreement can be produced by assuming slightly larger g -values of 1.46 for Dy^{3+} and 1.38 for Ho^{3+} . At lower temperature, the $\chi(T) \cdot T$ for Ti_4Ho_2 decreases smoothly, indicating likely antiferromagnetic exchange interactions between the nearby Ho^{3+} ions. Ti_4Dy_2 shows more complicated behaviour at low temperature, which may arise from a combination of magnetic exchange and magnetic anisotropy.

However, comparison of field-cooled (FC) and zero-field cooled (ZFC) magnetisation vs. temperature curves show no splitting in either compound (Fig. 5c), implying the absence of significant magnetic memory or slow magnetic relaxation. Similarly, magnetic hysteresis loops ($M(H)$) collected at 1.8 K show no measurable hysteresis (Fig. 5b). Interestingly, the Ti_4Dy_2 $M(H)$ shows sharp saturation behaviour with a saturated moment μ_{sat} of $5.5 \mu_{\text{B}}$, which is half that of the expected value for free (isotropic) Dy^{3+} ions ($\mu_{\text{sat}} = g \cdot J = 11.0 \mu_{\text{B}}$). This halving is commonly seen in powder samples of Dy^{3+} com-

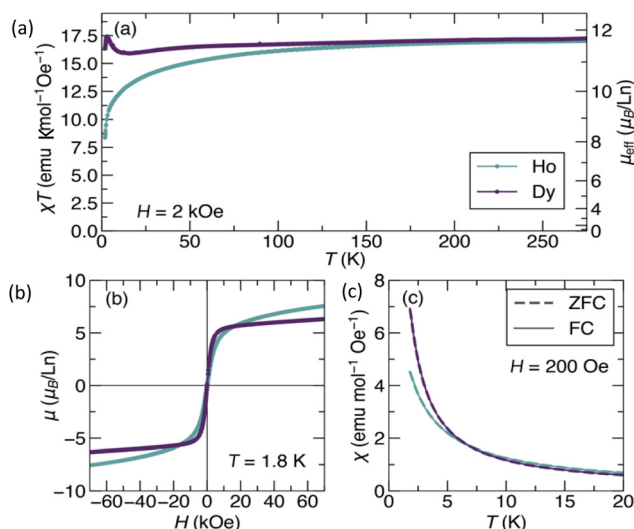


Fig. 5 (a) χT vs. temperature plots for Ti_4Ho_2 and Ti_4Dy_2 (powder), showing a room temperature effective moment μ_{eff} of about $11.7 \mu_{\text{B}}$ per lanthanide for both complexes. (b) Magnetisation vs. field hysteresis loops taken between 70 and -70 kOe (sweep rate = 100 Oe s^{-1}) at 1.8 K, showing a saturated moment of $\mu_{\text{sat}} = 7.6 \mu_{\text{B}}$ and $5.5 \mu_{\text{B}}$, respectively. Neither compound shows measurable hysteresis. (c) Magnetisation vs. temperature for both compounds, measured under both zero-field-cooled (ZFC) and field-cooled (FC) conditions in an applied field of 200 Oe. Neither compound shows a measurable difference between the ZFC and FC curves, indicating fast magnetic relaxation across the temperature range. In (a) and (c), susceptibility is expressed per mol of Ln^{3+} (rather than mol of Ln_2Ti_4 clusters).

pounds with strong uniaxial anisotropy, where powder averaging of the randomly oriented Ising-like spins reduces the moment by $\frac{1}{2}$ compared to the free-spin value. However, Ti_4Dy_2 does not appear to satisfy this condition as the molecular Dy...Dy vectors are not aligned in the same direction in the lattice (Fig. 6). The Ti_4Ho_2 compound shows a saturated

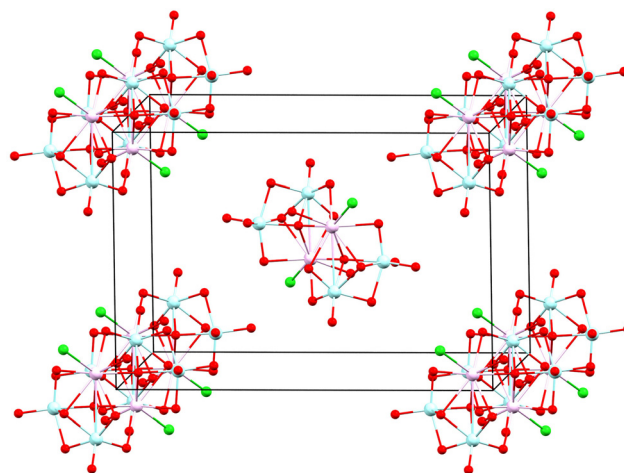


Fig. 6 Packing of Ti_4Dy_2 within the unit cell, in which the Dy...Dy axes are not aligned in the same direction (Ln = pink, Ti = blue, O = red, Cl = green).



moment around $7.6\mu_B$, somewhat lower than the free spin value of $11.04\mu_B$.

To examine the possibility of slow magnetic relaxation further, we performed AC susceptibility measurements at temperatures between 1.8 K and 10 K and frequencies between 10^{-1} Hz and 10^3 Hz. For both **Ti₄Dy₂** and **Ti₄Ho₂** no resonance was observed (ESI, Fig. S8†). The magnetic relaxation time is therefore assumed to be faster than 0.001 s, and neither compound can be considered to be single-molecule magnets. A possible reason for this is the long Ln...Ln distance (*ca.* 3.676 Å) and the resulting changes to the crystal field in **Ti₄Ln₂**.²³ While we have not measured the magnetic properties of the other lanthanide clusters, the lack of slow magnetic relaxation in these two clusters (especially **Ti₄Dy₂**) implies that the other members are unlikely to show slow magnetic relaxation.

Decomposition studies

The decomposition of the previously reported and novel Ln-POT cages prepared in the current study was analysed using two different strategies. In the first, the crystalline compounds were heated to 800 °C under an inert atmosphere of N₂, and their decomposition was monitored *via* thermogravimetric analysis (TGA). A distinct process of mass loss is observed for each structural type, irrespective of the Ln³⁺ ion present (ESI, Fig. S9†). Fig. 7 shows representative TGA traces for the thermal decomposition of selected cages.

For the smallest **Ti₄Ln₂** cages decomposition starts at around 150 °C in all cases, with the total mass loss occurring at around 350 °C due to the loss of all ethoxy ligands. As this series of compounds already shows a condensation ratio (O:Ti) of 2:1 (the same as that in TiO₂), this indicates the direct decomposition into titania. Although the decomposition of **Ti₂₈La** commences at a similar temperature to that of the

Ti₄Ln₂ cages a lower and more gradual total mass loss is seen, which is attributed to the lower condensation ratio of 1.4:1 (*i.e.*, far off that of TiO₂). The **Ti₈Er** cage has an even lower ratio of 0.9:1 leading to greater thermal stability compared to **Ti₂₈La** and the **Ti₄Ln₂** cages, with decomposition commencing at a higher temperature of around 250 °C.¹³ EDX data confirm the retention of chloride in the decomposition products of the **Ti₄Ln₂** cages. As no chloride ligands are present in the structure of **Ti₈Er** a very different decomposition mechanism is likely. All the solid-state materials obtained by thermolysis under N₂ at 800 °C were found to be amorphous by powder X-ray diffraction, which made further analysis of the phases difficult.

The second decomposition strategy involved hydrolytic treatment of the crystalline Ln-POT cages with a EtOH/H₂O solution, followed by annealing of the powders formed under air. The thermal removal of organic residues proved to be essential for successful characterisation of the products. As indicated by elemental (C, H) analysis, heating to 500 °C (12 h) was found to be sufficient for this purpose. However, crystalline materials (essential for characterisation by powder X-ray diffraction) were only obtained at higher temperature (800 °C). Analysis of these crystalline materials by SEM (Scanning Electron Microscopy) shows sharp-edged particles with an average size of >100 μm (Fig. 8 and S11–S17†). The surfaces appear to be smooth but show surface features at higher magnification. Earlier reports have described the formation of agglomerates of nanoparticles by room-temperature hydrolysis of Ln-POTs under sonication conditions, which was not the

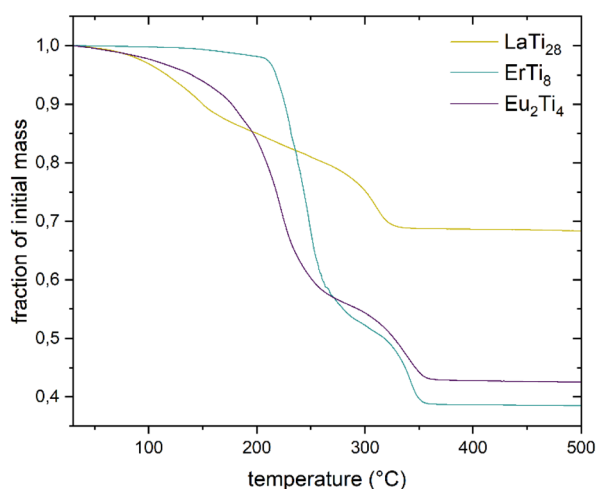


Fig. 7 TGA curves under nitrogen for the three different structural types of Ln-POTs. The measurements were carried out up to 800 °C at a heating rate of 10 °C min⁻¹, but mass loss was found to be completed at 500 °C in all cases.

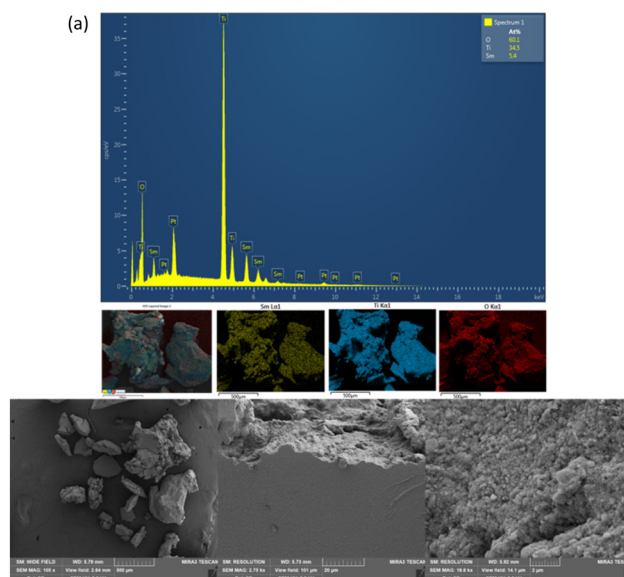


Fig. 8 (a) EDX map spectrum recorded at 15 kV of Sm₂Ti₂O₇/TiO₂ after annealing to 800 °C, showing a uniform elemental distribution across the sample (Sm in yellow, Ti in blue, O in red). The sample was sputtered with Pt prior to measurement. (b) SEM images of the same sample taken at different viewing fields (2.5 mm, 100 μm and 15 μm) with a 5 kV electron beam.



case in the current study due to the different decomposition conditions.¹⁶

Analysis of the decomposition products obtained by this route (annealed to 800 °C) was carried out using Raman spectroscopy, synchrotron XRD and EDX. For the **Ti₄Ln₂** series and **Ti₈Er** the formation of TiO₂ (anatase and rutile)/Ln₂Ti₂O₇ (pyrochlore-like) mixtures is expected based on the limited previous reports.^{15,16,18} A varying degree of crystallinity across the series of the decomposition products leads to differences in resolution of the spectra. However, Raman spectra confirm the presence of anatase in all of the decomposition products of **Ti₄Ln₂** and **Ti₈Er**, with characteristic peaks at around 144, 197, 399, 516 and 639 cm⁻¹ (ESI, Fig. S10†).²⁴ Since the anatase phase exhibits an unusually high degree of thermal stability, low-level Ln-doping is assumed for all samples. In some cases (**Ti₄Ln₂**, Ln = Gd, Tb, Dy; **Ti₈Er**) the appearance of a weak band at around 300 cm⁻¹ was also observed which can be assigned to the O–Ln–O bending mode of the respective pyrochlore-like phases.²⁵ For Ln = Ce, Nd, Tm (**Ti₄Ln₂**) and **Ti₈Er** more complex spectra were obtained than for the other precursors, which it was assumed result from the presence of multiple crystalline phases.

To quantify the suggested compositions, high-resolution synchrotron powder diffraction patterns were measured and the data were analysed by Rietveld refinement (Table 1). For all samples apart from the decomposition products of **Ti₂₈La**, **Ti₄Ce₂** and **Ti₄Nd₂**, titania/pyrochlore-like mixtures were obtained, as expected from Raman studies. The ratios of anatase and rutile vary across all the decomposition products depending on the lanthanide. This indicates different degrees of stabilisation of the anatase phase caused by low-level doping with Ln³⁺. In general, a large ionic radius of Ln³⁺ is reported to efficiently inhibit the anatase-to-rutile transition through the formation of Ti–O–Ln bonds.⁵ Therefore, only the anatase phase is observed for the decomposition product of **Ti₂₈La**. The decomposition of **Ti₄Ce₂** is reported to give Ce₂Ti₂O₇ (stabilised by a titania coating), which forms at

150 °C, but is found in the current study to decompose into Ce^{IV}O₂ and Ce^{IV}Ti₂O₆ (brannerite) upon heating to 800 °C.¹⁴ Further analysis of this monoclinic brannerite phase has shown that the stoichiometry is Ce_{0.975}Ti₂O_{5.95}, in which oxygen vacancies at the O1 site lead to charge compensation through Ce⁴⁺ vacancies.²⁷ No oxidation of Nd³⁺ occurs in the decomposition of **Ti₄Nd₂**, but the large ionic radius impedes the formation of a high-symmetry pyrochlore-like structure, thus orthorhombic Nd₄Ti₉O₂₄ is formed (Fig. 9).⁵

Previous studies suggest that Nd₄Ti₉O₂₄ consists of a 9 : 2 ratio of TiO₂ : Nd₂O₃, which is usually formed by a Nd₂Ti₂O₇ intermediate in high-temperature solid-state reactions.²⁸ For the rest of the **Ti₄Ln₂** series (Ln = Sm–Yb) cubic pyrochlore-like Ln₂Ti₂O₇ were formed in varying degrees, depending on the lanthanide. In general, partial site-mixing between the Ti and Ln positions is observed in Ln₂Ti₂O₇ with Ti⁴⁺ occupying some of the Ln³⁺ sites and *vice versa* (Table S8†), suggesting variable formation of the fluorite phases. However, a particularly low pyrochlore content (13.2 wt%) with no site-mixing is observed in the decomposition product of **Ti₈Er**, which is attributed to

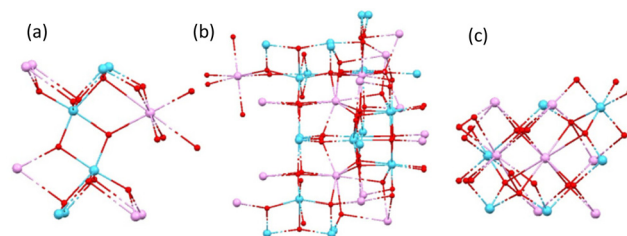


Fig. 9 Crystal structures of (a) Ce_{0.975}Ti₂O_{5.95}, (b) Nd₄Ti₉O₂₄ and (c) Sm₂Ti₂O₇. In each case the Ln³⁺ ions are coordinated by eight oxygen ions. The space group changes from monoclinic *C2/m* for brannerite to orthorhombic face-centred *Fddd* for the Nd–Ti oxide and then cubic face-centred *Fd3m* for the pyrochlores. Structural data were obtained from the ICSD (193469, 72316, 24208). (Ln = pink, Ti = blue, O = red).

Table 1 Phase composition of the hydrolytically decomposed materials obtained from Rietveld refinements (TOPAS-Academic package v.4.1)²⁶ and EDX. The predicted atomic percentages were calculated from the composition obtained from refinement of the powder diffraction data. EDX results are shown as the average of several point and map spectra across each sample

Ln	Rietveld refinement			Ln (at%)		Ti (at%)		O (at%)	
	Anatase (wt%)	Rutile (wt%)	Ln _x Ti _y O _z (wt%)	Calcd	EDX	Calcd	EDX	Calcd	EDX
La ^a	100	0	0	0	0.3	33.3	33.3	66.7	66.7
Ce ^{b,d}	0	17.7	70.0	12.8	6.4	12.8	15.7	72.3	78.0
Nd ^b	65.7	0	34.3	3.7	3.0	30.0	26.3	65.6	70.7
Sm ^b	11.2	23.4	65.4	11.9	4.5	23.3	28.8	64.5	66.8
Eu ^b	0	0	100.0	18.2	14.4	18.2	17.4	63.6	68.3
Gd ^b	74.2	0	25.8	4.7	3.6	29.2	23.5	65.4	73.0
Tb ^b	45.3	9.4	45.3	8.2	3.6	26.3	17.7	64.9	78.5
Dy ^b	0	23.1	76.9	14.0	9.5	21.6	18.8	64.2	71.8
Ho ^b	62.2	0	37.8	6.9	3.8	27.4	24.4	65.7	71.8
Er ^c	82.9	3.9	13.2	2.4	2.1	31.0	30.7	65.7	67.2
Tm ^b	22.5	22.6	54.9	10.0	8.5	24.9	19.3	64.7	72.3
Yb ^b	57.5	8.0	34.5	6.3	5.5	27.9	25.0	65.2	65.5

^a From **Ti₂₈La**. ^b From **Ti₄Ln₂**. ^c From **Ti₈Er**. ^d The remaining 12.3% is CeO₂.



the Ti : Er stoichiometry in the precursor and the resulting preference to form Er-doped anatase (82.9 wt%).

EDX analysis of all the decomposition products shows a uniform elemental distribution across the series of lanthanides (Fig. 8, ESI Figs. S18 and S19†). Atomic percentages of Ln, Ti and O were obtained from multiple map and point spectra per sample. The mean results were compared to those calculated from the composition obtained from the Rietveld refinements (Table 1). In general, the calculated and experimental percentages match reasonably well, however, in some cases the oxygen contents lie significantly above the values obtained from the Rietveld refinements, leading to underestimation of the metal content by EDX. It has previously been reported that particles obtained by decomposition of Ln-POTs have a higher concentration of TiO₂ on their surfaces, which could account for the low Ln content measured in some cases since EDX is a surface technique.¹⁵ In addition, since EDX measurements only have limited detection accuracy for light elements, the oxygen percentages determined here should be interpreted with care.

Band gap determination

The band gaps of the materials produced by decomposition of the Ln-POTs at 800 °C in air were estimated by linear extrapolation of the solid-state UV-Vis spectra (Fig. 10b).²⁹ The results were compared to the HOMO-LUMO gaps of the Ln-POT cages obtained from both solution (Fig. 10a) and solid-state (ESI Fig. S22†) UV-Vis spectra (Table 2). The results obtained by linear extrapolation of the cages in the solid state and of the solid decomposition products are similar to those found using Tauc plots, with the values from direct extrapolation being generally higher by *ca.* 0.2 eV (ESI, Table S9†). Similar observations were made previously in our comparison of bandgap determination using direct extrapolation or Tauc plots.²⁹ It can be noted that the best fits of the data for the decomposition products are obtained in Tauc plots with an exponent of $\frac{1}{2}$, suggesting direct (allowed) band gap behaviour.

As shown in Fig. 10a the absorption maxima of the Ln-POTs in DCM are blue-shifted compared to the starting material Ti(OEt)₄ (245 → 229 nm).³⁰ The larger **Ti₂₈La** cluster gives a high HOMO-LUMO gap of around 4.40 eV, whereas the smaller **Ti₄Ln₂** cages and **Ti₈Er** show slightly lower values. For the decomposed materials a broad UV-Vis absorption band around 300–400 nm is observed, which is attributed to the O(p) → Ti(d) charge-transfer transition in titania (Fig. 10b). Additional small peaks in the visible range depend on the electronic structure of the Ln³⁺ ions and their f-f transitions. When moving from discrete molecular energy levels (POTs) to the solid-state materials a general reduction of the band gap is observed. Most solid-state samples show band gaps similar to those of rutile and anatase. A large red shift is obtained for the decomposition product of **Ti₄Ce₂**, which is in agreement with literature.³¹ The HOMO-LUMO gaps obtained for the cages in the solid state lie between those from solution-state measurements and the band gaps of the decomposed materials. It is unclear, however, to what extent hydrolysis is responsible for

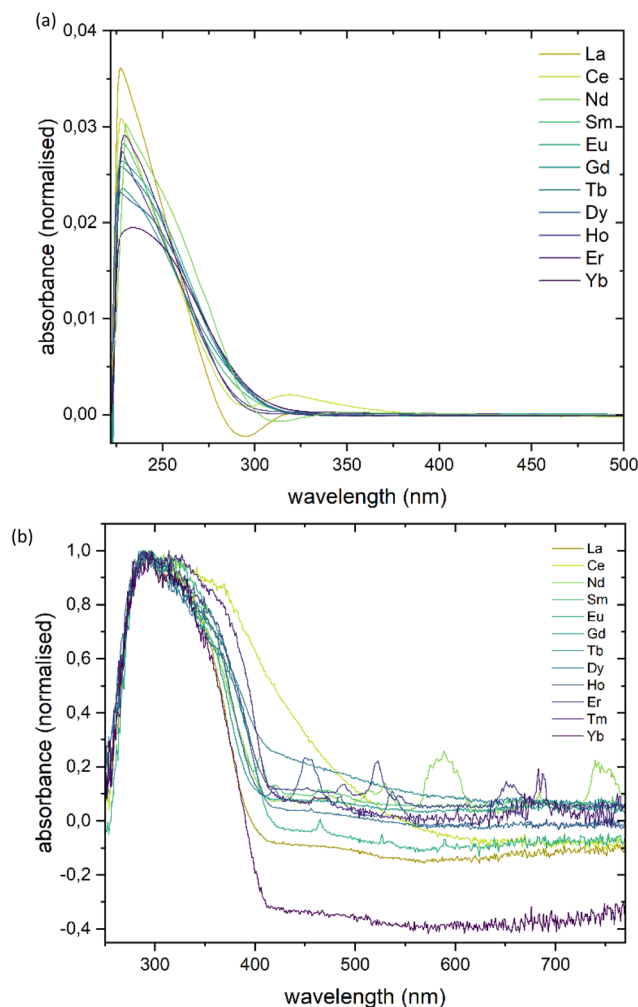


Fig. 10 (a) Solution-state UV-Vis spectra for the series of Ln-POTs in DCM. The samples were prepared under an inert atmosphere using anhydrous DCM (0.033 mg mL⁻¹). (b) Solid-state UV-Vis reflectance spectra for the hydrolytically decomposed materials. In both cases the spectra were normalised to allow better comparison of the influence of different lanthanides on the optical properties of the sample.

Table 2 Optical band gap data for both molecular Ln-POTs and hydrolytically decomposed Ln/TiO hybrid materials. The values were estimated based on UV-Vis absorbance data

Ln	HOMO-LUMO gap solution-state (eV)	HOMO-LUMO gap solid-state (eV)	Solid-state band gap (eV)
La ^a	4.40	3.09	3.15
Ce ^b	4.29	2.95	2.38
Nd ^b	4.16	3.53	2.99
Sm ^b	4.21	3.42	3.03
Eu ^b	4.14	3.51	2.99
Gd ^b	4.10	3.44	3.08
Tb ^b	4.14	3.37	2.81
Dy ^b	4.10	3.36	2.98
Ho ^b	4.23	3.52	3.05
Er ^c	4.26	3.44	2.95
Tm ^b	— ^d	— ^d	2.94
Yb ^b	4.07	3.27	3.17

^a From **Ti₂₈La**. ^b From **Ti₄Ln₂**. ^c From **Ti₈Er**. ^d Not enough sample was obtained.



this as the cages in the solid state could not be measured under inert atmosphere.

Conclusions

Following on from earlier reports on selected Ln-POTs,^{14–16,18} in this work we have investigated an expanded series of Ln-POTs and their potential use as single-source precursors for lanthanide/titanium oxide materials. Structural analysis of the cages showed a dependency of the nuclearity on both the size of the Ln³⁺ ion and the reaction conditions. Assessment of the magnetism of **Ti₄Dy₂** and **Ti₄Ho₂** shows that both compounds are not single molecule magnets. Upon hydrolytic decomposition of the cages Ln₂Ti₂O₇ pyrochlore-like compounds were obtained for **Ti₈Ln** and **Ti₄Ln₂**-type POTs, while lower Ln:Ti ratios (**Ti₂₈La**) formed lanthanide-doped titania. The presence of lanthanide ions led to efficient inhibition of the anatase-to-rutile transition at temperatures up to 800 °C. For Ce and Nd-containing precursors annealing of the hydrolytically decomposed samples led to the formation of different phases (Ce(IV)-oxidation products and orthorhombic Nd₄Ti₉O₂₄, respectively). Only for the decomposition product of **Ti₄Ce₂** at 800 °C in air (consisting of Ce^{IV}O₂ and Ce^{IV}Ti₂O₆) was a significant reduction of the band gap observed from that of titania (3.20 → 2.38 eV).

Overall, this work shows that single-source Ln-POTs have promising applications in the synthesis of pyrochlore-like composite materials. Analysis of the photocatalytic properties of the solid-state Ln–Ti oxide decomposition products would be of interest in future studies to assess the impact of different forms of lanthanide-doping further.

Experimental section

General remarks

All experimental procedures were carried out under a dry inert atmosphere of N₂ with the aid of a vacuum-line and glovebox (Saffron, type-α) unless specified otherwise. Starting materials and dry alcohols were purchased from suppliers (Fischer Scientific, Alpha Aesar, Merck) and used as received. Lanthanide(III) chlorides were obtained as anhydrous salts. Elemental analysis was performed using a PerkinElmer 240 Elemental Analyser, with samples (1–2 mg) being sealed in one-piece tin tubes in the glovebox before analysis. IR spectra were acquired on a Thermo Scientific Nicolet iS50 FT-IR in ATR mode. TGA data were acquired on a Mettler Toledo TGA/DSC. SEM/EDX measurements were carried out on a Tescan MIRA3 SEM under vacuum. The samples were deposited on carbon tape and sputtered with 10 nm Pt prior to measurement. UV-Vis spectra were measured using a VARIAN Cary 50 Bio UV-Visible spectrometer (solution) or an Aligent Cary 60 UV-Vis spectrophotometer with external light source/detector (solid state). Solution UV samples were prepared under nitrogen in a glovebox. Raman spectroscopy was carried out using a

Renishaw inVia Raman Microscope (532 nm laser source). Magnetic measurements were acquired using a Quantum Design cryogen-free Magnetic Property Measurement System (MPMS). Standard powder sample holders (brass) were used. Samples were maintained under a nitrogen atmosphere throughout the measurements. Single-crystal X-ray diffraction data were collected using a Bruker D8-QUEST PHOTON-III (Incoatec IμS Cu microsource) diffractometer. The temperature was held at 180 K using an Oxford Cryosystem N₂ cryostat. Structures were solved using SHELXT³² and refined using SHELXL.³³ In-house pXRD analysis was carried out on a Panalytical XPert Pro diffractometer (using Cu radiation, 1.5406 Å). High resolution powder XRD data were collected at the Diamond Light Source Synchrotron i11 beamline using a wavelength of 0.82443 Å. In-house powder XRD samples were protected from ambient air by being sandwiched between two Kapton sheets. High-resolution synchrotron pXRD samples were prepared in glass cannulae and sealed with glue. Single-crystal X-ray data has been deposited with the Cambridge Crystallographic Data Base (deposition numbers 2283715–2283722†).

Ln-POT synthesis

The La, Ce, Nd, Eu and Er-containing POTs were synthesised as described in the literature for reasons of completeness.^{14–16,18}

Under a dry inert atmosphere of N₂, Ti(OEt)₄ (3.5 mL, 16.7 mmol) was added to a suspension of LnCl₃ (1.7 mmol) in anhydrous ethanol (7 mL) and sealed in a 12 mL Teflon-lined autoclave. After heating to 150 °C for 3 days the reaction was slowly cooled to room temperature (1–10 °C min^{−1}). The resulting solution was kept at −30 °C until a crystalline product had formed. After removal of the mother liquor the crystals were washed with anhydrous ethanol (2 × 3 mL) and *n*-pentane (1 × 3 mL) and dried under reduced pressure.

[{Ti₂O(OEt)₈}(EtOH-SmCl)]₂ pale yellow needles (21% wrt Sm). Elem. anal; calcd C, 30.7, H, 6.6. Found C, 30.8, H, 6.8. Important IR data (KBr, cm^{−1}): 2968(s), 2922(s), 2863(s), 1376(vs), 1127(s), 1086(s), 1044(s), 888(s).

[{Ti₂O(OEt)₈}(EtOH-GdCl)]₂ colourless block-shaped crystals (16% wrt Gd). Elem. anal; calcd C, 30.4, H, 6.5. Found C, 30.5, H, 6.8. Important IR data (KBr, cm^{−1}): 2966(s), 2921(s), 2862(s), 1627(w), 1376(vs), 1127(s), 1085(s), 1044(s), 890(s).

[{Ti₂O(OEt)₈}(EtOH-TbCl)]₂ colourless needles (12% wrt Tb). Elem. anal; calcd C, 30.3, H, 6.5. Found C, 29.6, H, 7.0. Important IR data (KBr, cm^{−1}): 2967(s), 2922(s), 2862(s), 1376(vs), 1127(s), 1087(s), 1045(s), 892(s).

[{Ti₂O(OEt)₈}(EtOH-DyCl)]₂ pale blue block-shaped crystals (9% wrt Dy). Elem. anal; calcd C, 30.2, H, 6.5. Found C, 29.8, H, 6.6. Important IR data (KBr, cm^{−1}): 2968(s), 2922(s), 2862(s), 1378(vs), 1127(s), 1085(s), 1045(s), 890(s).

[{Ti₂O(OEt)₈}(EtOH-HoCl)]₂ pink needles (10% wrt Ho). Elem. anal; calcd C, 30.1, H, 6.4. Found C, 28.6, H, 6.3. Important IR data (KBr, cm^{−1}): 2969(s), 2922(s), 2862(s), 1378(vs), 1127(s), 1085(s), 1045(s), 890(s).



$[\{\text{Ti}_2\text{O}(\text{OEt})_8\}(\text{EtOH-TmCl})]_2$ colourless needles (1.2% wrt Tm). Elem. anal. unsuccessful due to insufficient amount of sample.

$[\{\text{Ti}_2\text{O}(\text{OEt})_8\}(\text{EtOH-YbCl})]_2$ colourless block-shaped crystals (11% wrt Yb). Elem. anal; calcd C, 29.8, H, 6.4. Found C, 29.4, H, 6.4. Important IR data (KBr, cm^{-1}): 2967(s), 2923(s), 2861(s), 1377(vs), 1126(s), 1089(s), 1046(s), 892(s).

Hydrolytic decomposition

The obtained crystalline Ln-POTs (300–400 mg) were dissolved in DCM (5 mL) and added dropwise to a stirred solution of ethanol (10 mL) and water (10 mL). Stirring was continued overnight and after phase separation the organic layer was discarded. The white to off-white precipitate was dried under reduced pressure to give the initial products (150–200 mg). The amorphous powders were heated to temperatures between 350–800 °C to remove organic residues and induce crystallisation.

Conflicts of interest

There are no conflicts of interest to declare.

Acknowledgements

We would like to thank Dr. Cheng Liu (Maxwell Centre Cambridge) for his technical support at the SQUID magnetometer and Dr Chloe Coates for her input on the Rietveld analysis. We also acknowledge I11 beamline for synchrotron XRD under the BAG proposal (CY28349). The authors would like to thank the Todd-Hamied fund (Cambridge) and the Cusanuswerk e.V. for financial support.

References

- X. Chen and S. Mao, *Chem. Rev.*, 2007, **107**, 2891; A. Fujishima and K. Honda, *Nature*, 1972, **238**, 37; J. Disegi and H. Wyss, *Orthopedics*, 1989, **12**, 75.
- H. Macleod, *Thin film optical filters*, MacMillan, New York, 1986, p. 370; A. Linsebigler, G. Lu and J. Yates, *Chem. Rev.*, 1995, **95**, 735; A. Hagfeldt and M. Grätzel, *Chem. Rev.*, 1995, **95**, 49; P. Moseley and B. Tofield, *Solid state gas sensors*, Adam Hilger, Bristol, 1987; A. Alivisatos, *Science*, 1996, **271**, 933.
- H. Tang, K. Prasad, R. Sanjines, P. E. Schmid and F. Levy, *J. Appl. Phys.*, 1994, **75**, 2024.
- K. E. Karakitsou and X. E. Verykios, *J. Phys. Chem.*, 1993, **97**, 1184; V. Augugliaro, L. Palmisano, M. Schiavello and A. Scafani, *J. Phys. Chem.*, 1991, **95**, 274.
- Y. Zhang, H. Zhang, Y. Xu and Y. Wang, *J. Solid State Chem.*, 2004, **177**, 3490.
- S. Yuan, Q. Sheng, J. Zhang, F. Chen, M. Anpo and Q. Zhang, *Microporous Mesoporous Mater.*, 2005, **79**, 93; T.-D. Nguyen-Phan, M. B. Song, E. J. Kim and E. W. Shin, *Microporous Mesoporous Mater.*, 2009, **119**, 290.
- K. T. Ranjit, I. Willner, S. H. Bossmann and A. M. Braun, *Environ. Sci. Technol.*, 2001, **35**, 1544.
- Y.-H. Zhang and A. Reller, *J. Mater. Chem.*, 2001, **11**, 2537; M. Martos, B. Julián-López, J. V. Folgado, E. Cordoncillo and P. Escribano, *Eur. J. Inorg. Chem.*, 2008, 3163; L. H. Brixner, *Inorg. Chem.*, 1964, **3**, 1065.
- (a) M. A. Subramanian, G. Aravamudan and G. V. S. Rao, *Prog. Solid State Chem.*, 1983, **15**, 55; (b) A. F. Fuentes, S. M. Montemayor, M. Maczka, M. Lang, R. C. Ewing and U. Amador, *Inorg. Chem.*, 2018, **57**, 12093.
- A. V. Prasadara, U. Selvaraj, S. Komarneni and A. S. Bhalla, *J. Mater. Res.*, 1992, **7**, 2859.
- P. Berdowski and G. Blasse, *J. Solid State Chem.*, 1986, **62**, 317; P. Dasgupta, Y. M. Jana, A. Nag Chattopadhyay, R. Higashinaka, Y. Maeno and D. Gosh, *J. Phys. Chem. Solids*, 2007, **68**, 347; G. Luo, S. Hess and L. R. Corruccini, *Phys. Lett. A*, 2001, **291**, 306; P. Bonville, S. Petit, I. Mirebeau, J. Robert, E. Lhotel and C. Paulsen, *J. Phys.: Condens. Matter*, 2013, **25**, 275601; L.-J. Chang, S. Onoda, Y. Su, Y.-J. Kao, K.-D. Tsuei, Y. Yasui, K. Kakurai and M. R. Lees, *Nat. Commun.*, 2012, **3**, 992; T. Fennell, P. P. Deen, A. R. Wildes, K. Schmalzl, D. Prabhakaran, A. T. Boothroyd, R. J. Aldus, D. F. McMorrow and S. T. Bramwell, *Science*, 2009, **326**, 415; D. J. P. Morris, D. A. Tennant, S. A. Grigera, B. Klemke, C. Castelnovo, R. Moessner, C. Czternasty, M. Meissner, K. C. Rule, J.-U. Hoffmann, K. Kiefer, S. Gerischer, D. Slobinsky and R. S. Perry, *Science*, 2009, **326**, 411.
- M. Veith, *J. Chem. Soc., Dalton Trans.*, 2002, 2405.
- S. Eslava, M. McPartlin, R. Thomson, J. Rawson and D. S. Wright, *Inorg. Chem.*, 2010, **49**, 11532.
- Y. Lv, J. Willkomm, M. Leskes, A. Steiner, T. C. King, L. Gan, E. Reisner, P. T. Wood and D. S. Wright, *Chem. – Eur. J.*, 2012, **18**, 11867.
- Y. Lv, M. Yao, J. P. Holgado, T. Roth, A. Steiner, L. Gan, R. M. Lambert and D. S. Wright, *RSC Adv.*, 2013, **3**, 13659.
- Y. Lv, Z. Cai, D. Yan, C. Su, W. Li, W. Chen, Z. Ren, Y. Wei, O. Mi, C. Zhang and D. S. Wright, *RSC Adv.*, 2016, **6**, 57.
- C. Artner, S. Kronister, M. Czakler and U. Schubert, *Eur. J. Inorg. Chem.*, 2014, 5596.
- Y. Lv, W. Du, Y. Ren, Z. Cai, K. Yu, C. Zhang, Z. Chen and D. S. Wright, *Inorg. Chem. Front.*, 2016, **3**, 1119.
- D.-F. Lu, Z.-F. Hing, J. Xie, X.-J. Kong, L.-S. Long and L.-S. Zheng, *Inorg. Chem.*, 2017, **56**, 12186.
- I. Tuvi-Arad, G. Alon and D. Avnir, *CoSym: Continuous Symmetry Measures*, 2018, <https://csm.ouproj.org.il/molecule>.
- D. Parker, E. A. Suturina, I. Kuprov and N. F. Chilton, *Acc. Chem. Res.*, 2020, **53**, 1520.
- N. F. Chilton, *Annu. Rev. Mater. Res.*, 2022, **52**, 79.
- C. A. Gould, K. R. McClain, D. Reta, J. G. C. Kragoskow, D. A. Marchiori, E. Lachman, E.-S. Choi, J. G. Analytis, R. D. Britt, N. F. Chilton, B. G. Harvey and J. R. Long, *Science*, 2022, **375**, 198.



- 24 A. Li Bassi, D. Cattaneo, V. Russo, C. E. Bottani, E. Barborini, T. Mazza, P. Piseri, P. Milani, F. O. Ernst, K. Wegner and S. E. Pratsinis, *J. Appl. Phys.*, 2005, **98**, 74305.
- 25 D. M. De los Santos, J. Navas, T. Aguilar, A. Sánchez-Coronilla, C. Fernández-Lorenzo, R. Alcántara, J. C. Pinero, G. Blanco and J. Martín-Calleja, *Beilstein J. Nanotechnol.*, 2015, **6**, 605.
- 26 A. Coelho, *Topas, v4.1*, Bruker AXS GmbH, Karlsruhe, Germany, 2003.
- 27 M. C. Stennett, C. L. Freeman, A. S. Gandy and N. C. Hyatt, *J. Solid State Chem.*, 2012, **192**, 172.
- 28 N. Hübner and R. Gruehn, *Z. Anorg. Allg. Chem.*, 1992, **616**, 86.
- 29 Y. Lv, J. Cheng, P. D. Matthews, J. P. Holgado, J. Willkomm, M. Leskes, A. Steiner, D. Fenske, T. C. King, P. T. Wood, L. Gan, R. M. Lambert and D. S. Wright, *Dalton Trans.*, 2014, **43**, 8679.
- 30 F. Babonneau, A. Leautic and J. Livage, *MRS Proc.*, 1988, **121**, 317.
- 31 L. Kumaresana, A. Prabhua, M. Palanichamy, E. Arumugam and V. Murugesan, *J. Hazard. Mater.*, 2011, **186**, 1183.
- 32 G. M. Sheldrick, *Acta Crystallogr., Sect. A: Found. Adv.*, 2015, **71**, 3–8.
- 33 G. M. Sheldrick, *Acta Crystallogr., Sect. C: Struct. Chem.*, 2015, **71**, 3–8.

